Unlocking Optical Coupling Tunability in Epsilon-Near-Zero Metamaterials Through Liquid Crystal Nanocavities

Giuseppe Emanuele Lio, Antonio Ferraro, Bruno Zappone,* Janusz Parka, Ewa Schab-Balcerzak, Cesare Paolo Umeton, Francesco Riboli, Rafał Kowerdziej, and Roberto Caputo**

Epsilon-near-zero (ENZ) metamaterials represent a powerful toolkit for selectively transmitting and localizing light through cavity resonances, enabling the study of mesoscopic phenomena and facilitating the design of photonic devices. In this experimental study, it demonstrates the feasibility of engineering and actively controlling cavity modes, as well as tuning their mutual coupling, in an ENZ multilayer structure. Specifically, by employing a high-birefringence liquid crystal film as a tunable nanocavity, the polarization-dependent coupling of resonant modes with narrow spectral width and spatial extent is achieved. Surface forces apparatus (SFA) allowed to continuously and precisely control the thickness of the liquid crystal (LC) film contained between the nanocavities and thus vary the detuning between the cavity modes. Hence, it is able to manipulate nanocavities anti-crossing behaviors. The suggested methodology unlocks the full potential of tunable optical coupling in epsilon-near-zero metamaterials and provides a versatile approach to the creation of tunable photonic devices, including bio-photonic sensors and/or tunable planar metamaterials for on-chip spectrometers.

1. Introduction

In the eighteenth century, the voltaic pile invented by Alessandro Volta demonstrated that stacking materials with different properties can lead to groundbreaking devices with significantly novel functionalities. Nowadays, this approach is recognized as a cornerstone of fabrication technology, particularly in the development of high-performance nano-devices. The Fabry-Perot resonator is one of the most convenient and broadly used devices in photonics, particularly for engineering light-matter coupling[1–3] and is commonly used in color filters,[4,5] two-photon direct laser writing with hyper-resolution,[6,7] optical metasurfaces,[8,9] high-heat release,[10,11] sensing devices,[12–14] and anti-counterfeiting tags,[15] just to name a few. The resonant cavity is usually fabricated by

---

G. E. Lio
Physics Department
University of Florence
Sesto Fiorentino, Florence 50019, Italy
E-mail: lio@lens.unifi.it

G. E. Lio, F. Riboli
European Laboratory for non Linear Spectroscopy (LENS)
Sesto Fiorentino, Florence 50019, Italy

A. Ferraro, B. Zappone, C. P. Umeton, R. Caputo
Consiglio Nazionale delle Ricerche - Istituto di Nanotecnologia (CNR-Nanotec)
Rende, CS 87036, Italy
E-mail: bruno.zappone@cnr.it; roberto.caputo@unical.it

The ORCID identification number(s) for the author(s) of this article can be found under https://doi.org/10.1002/adom.202302483

DOI: 10.1002/adom.202302483

J. Parka, R. Kowerdziej
Institute of Applied Physics
Military University of Technology
2 Kaliskiego Str., Warsaw 00-908, Poland

E. Schab-Balcerzak
Centre of Polymer and Carbon Materials Polish Academy of Sciences
34 M. Curie-Sklodowska Str., Zabrze 41-819, Poland

C. P. Umeton, R. Caputo
Physics Department
University of Calabria
Arcavacata di Rende, CS 87036, Italy

F. Riboli
National Institute of Optics
CNR-INO, Sesto Fiorentino, FI 50019, Italy

R. Caputo
Institute of Fundamental and Frontier Sciences
University of Electronic Science and Technology of China
Chengdu 610054, China

sandwiching a transparent dielectric layer between two partially reflecting mirrors. These metal-dieletric resonators possess the intriguing properties of epsilon-near-zero (ENZ) effective permittivity[16–18] at specific resonance wavelengths that can be finely tuned by carefully selecting the thickness and refractive index of the metal and dielectric layers, and the angle and polarization of the incoming light.[2] Multilayer resonators also allow to efficiently manipulate electromagnetic waves in specific spectral ranges and enable optimal solutions for device miniaturization,[19] fabrication of perfect absorbers for structural coloring in the VIS-NIR range,[20] and high photovoltaic conversion.[21] Furthermore, photon confinement in optical nanocavities enables an efficient control of light-matter coupling in fundamental physics studies of single quantum objects[22] and correlated polaritons,[23,24] as well as applications in quantum optical devices, and sensors.[25–29]

In this context, there is high demand of devices that can be reconfigured and adapted to various emerging technologies, especially in the automotive and telecommunication sectors.[30] Current ENZ metamaterial technologies, however, lack the ability to dynamically adjust their functionalities. Liquid crystals (LCs) show a large and fast response to external stimuli and are ideal candidates to overcome this limitation. For instance, elastomeric LCs have been used to tune photonic crystals[31] and Fabry-Perot cavities.[32] LC-based metasurfaces have also been recently implemented, confirming the extraordinary capabilities of LCs in the active control of visible light,[33–36] while extensions to the microwave[37,38] and terahertz regimes[39,40] are under way. The primary challenge to developing an active, LC-based ENZ metamaterial is to reduce the LC thickness to a few hundred nanometers. This thickness is considerably smaller than the limit of a few micrometers currently achieved in display technology.

In this article, we present experimental and numerical evidence of optical coupling in ENZ multilayer metamaterials comprising a nanoscale high-birefringence LC film with tunable thickness achieved by means of a Surface Force Apparatus (SFA). Originally designed to measure surface forces across fluid films,[41] the SFA has been recently introduced in photonics as a tool to control mode coupling in optical cavities.[24,42] Specifically, we have investigated a system comprising a nanoscale LC film (T-layer) with variable thickness d_T sandwiched between two identical metal-insulator-metal (MIM) cavities, thereby creating a symmetric three-cavity resonator denoted as MIMTMIM. The MIM cavities were fabricated by sputtering deposition on two cylindrical surfaces having a radius $R = 2$ cm. The surfaces were mounted with crossed axes in the SFA ensuring a single contact point (i.e., point of closest surface approach, $r = 0$ in **Figure 1**b) where the surface distance was d_T. Around this point, the distance h_T varied approximately as in a sphere-plane geometry: $h_T \approx d_T + r^2/2R$. The three-cavity resonator was illuminated with white light under normal incidence. The SFA allowed controlling the LC thickness dynamically, accurately, and continuously from several tens of microns down to the direct mechanical contact between the MIM surfaces (Figure 1a). Details about the SFA technique are provided in the Experimental Section and a Scheme is shown as Supporting Information (Figure S1, Supporting Information).

2. Mode Coupling in a Multi-Cavity Resonator

Let us begin the theoretical considerations with the analysis of multi-beam interference under normal incidence in a single (Fabry-Perot) MIM cavity constituted by an isotropic material (I-layer). A plane wave resonates with a cavity if the following condition of constructive interference occurs:[43,44]

$$n_T K_q d_T = q\pi - \phi \tag{1}$$

where n_T is the refractive index of the cavity medium, d_T is the metal–metal surface separation distance, q is the resonance order, $K_q = 2\pi/\lambda_q$ is resonance wavevector with wavelength λ_q, and ϕ is the phase shift due to reflection at the dielectric-metal interface. Both n and ϕ vary slowly with the wavelength and can be considered approximately constant across the ≈ 100 nm spectral range of an SFA experiment. The resonance condition Equation (1) can thus be rewritten as:

$$\lambda_q = 2n_T d_T/(q - \phi/\pi) \tag{2}$$

showing that the resonance wavelength λ_q increases linearly as the surface distance d_T or the refractive index n_T increases, whereas it decreases when the order number q increases. The transmittance of a MIM cavity under normal incidence can be accurately calculated as a function of wavelength λ and the cavity thickness using the transfer matrix multiplication (TMM) method (green lines in Figure 1c). For the MIM cavities considered in our experiments, only one resonance wavelength $\lambda_1 = 560$ nm appeared in the SFA spectral range. The TMM calculation showed that λ_1 corresponded to the first resonant mode obtained for the MIM cavity thickness of $d_1 = 95$ nm (horizontal dashed red line in Figure 1c).

In a three-cavity MIMTMIM resonator, a cavity mode can overlap and interfere with the resonances of neighboring cavities across the metal (M) layers. Consequently, the coupling of resonances and the optical interaction among the cavities that give rise to hybrid resonance modes.[42] A three-cavity resonator with a variable thickness d_T of the central cavity (T-layer) and fixed thickness d_1 of the outer cavities (I-layers) resonates at three different wavelengths (λ_L, λ_1, and λ_U in Figure 1c), related to the resonances of the three cavities. The dispersion of a symmetric three-cavity resonator has been studied in detail in ref. [42] and will be discussed in Section IV. Briefly, the dependence of the wavelength triplet (λ_L, λ_1, and λ_U) on d_T reflects the hybridization and avoided crossing between equal-symmetry modes of the inner and outer cavities. Namely, the avoided-crossing point corresponds to the thickness d_T at which the inner cavity should resonate at the same wavelength λ_1 as the outer cavities. Interestingly, λ_L and λ_U depend on d_T, whereas λ_1 is constant. Far from the avoided-crossing point, λ_L is close to the resonant wavelength of the inner cavity, while λ_U is close to the constant wavelength λ_1, or vice versa. Therefore, λ_L or λ_U increases almost linearly with the inner cavity thickness following Equation (1).

Because resonance modes sense both cavity thickness and refractive index, filling the inner cavity with a birefringent LC material leads to the doubling of resonance modes (e.g., $\lambda_L o$ and $\lambda_L e$ for the ordinary and extraordinary polarization, respectively, Figure 1c). These preliminary considerations highlight the

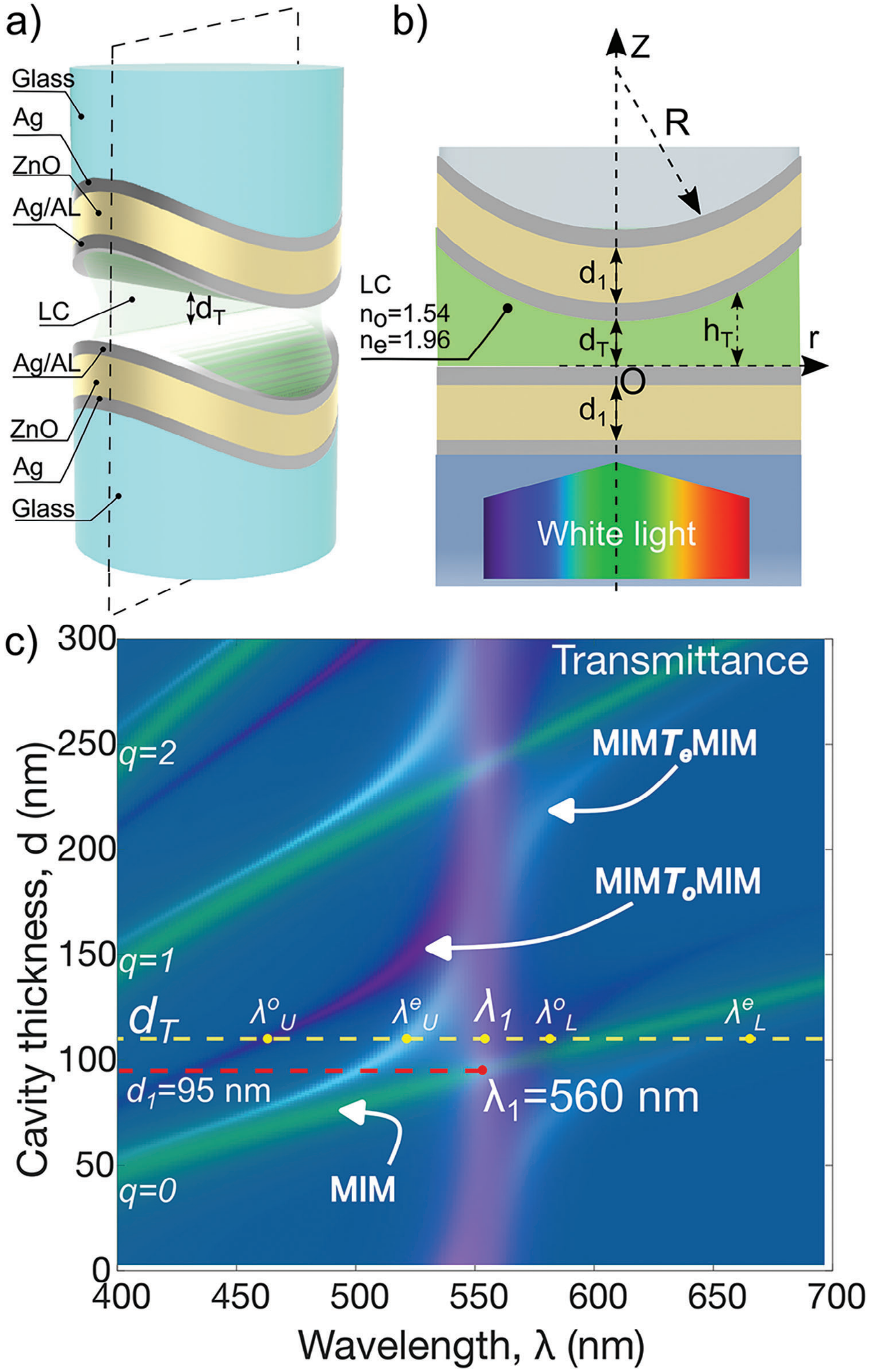
a)
Glass
Ag
ZnO
Ag/AL
LC
dT
Ag/AL
ZnO
Ag
Glass
b)
Z
R
d1
LC
no=1.54
ne=1.96
dT
hT
r
O
d1
White light
c)
Transmittance
MIMTeMIM
MIMToMIM
q=2
q=1
q=0
dT
λoU
λeU
λ1
λoL
λeL
d1=95 nm
λ1=560 nm
MIM
Cavity thickness, d (nm)
0
50
100
150
200
250
300
400
450
500
550
600
650
700
Wavelength, λ (nm)

Figure 1. a) Illustration of the three-cavity MIMTMIM resonator realized in the SFA. A ZnO layer (I) sandwiched between two Ag layers (M) with equal thickness constitutes a MIM cavity and was deposited by sputtering on each of the two cylindrical glass lenses of the SFA. LC film (T) confined between the MIM cavities forms a third cavity with non-uniform thickness. b) Cross-section view of the SFA geometry with the *z* direction of light incidence is evidenced. The geometry of the two cylindrical surfaces is approximated by a plane and a sphere with *r* being the lateral distance from the contact point ($r = 0$). h_T and d_T are respectively the surface distances at a given *r* and at $r = 0$. c) Transmittance under normal incidence calculated using the TMM method for a MIM cavity (green lines) as as function of the wavelength λ and thickness of the I-layer, and for the three-cavity resonator as a function of λ and thickness d_T of the LC film (T-layer), for both ordinary (MIMT$_o$MIM, purple curves) and extraordinary polarizations (MIMT$_e$MIM, cyan curves). A resonance corresponds to a local intensity maximum. λ_1 is the first-mode wavelength of the MIM cavity obtained for the thickness d_1. In addition to λ_1, four different wavelengths $\lambda_{U,L}^{o,e}$ are obtained at the LC thickness d_T marked with a yellow horizontal line, where *o* and *e* indicate the given polarization and *U* and *L* denote the (lower/upper) photon energy relative to λ_1.

potential of birefringent materials for tuning the resonances of metal-dielectric metametarials. On the other hand, when the T-layer is an optically anisotropic LC film, these wavelengths depend on light polarization (purple and cyan curves in Figure 1c).

3. Experimental Results

In the realized system, the thickness of silver (Ag, M-layers) and zinc oxide (ZnO, I-layers) is 30 and 95 nm, respectively. The LC material considered for the T-layer is a high-birefringence nematic liquid crystal mixture named LC1825, synthesized by the Military University of Warsaw[45] with a birefringence of $\Delta n = n_e - n_o = 0.42$, where $n_e = 1.96$ and $n_o = 1.54$ are the extraordinary and ordinary refractive indices at room temperature, respectively. The photoalignment compound JK158[46] was spin-coated on the Ag surfaces facing the LC to induce planar orientation along the cylinder axis on one surface and perpendicular to the axis on the other surface. Crossing the axes in the SFA ensured a planar alignment uniform across the LC thickness. Therefore, polarized parallel or perpendicular to the LC orientation travelled in the LC film as purely extraordinary or ordinary waves, respectively. Further details on the fabrication and materials used in our experiments are provided in the Experimental Section. During the experiment, a collimated white-light beam coming from a halogen lamp illuminated the MIMTMIM resonator under normal incidence and the transmitted intensity was analyzed using an imaging spectrograph coupled to a high-resolution CCD camera. In the spectrogram of **Figure 2**, the transmitted intensity *I* was measured as a 2D function of the wavelength λ and lateral distance *r* for the contact point ($r = 0$ in Figure 1). A resonance produces a local maximum in the intensity function $I_0(r, \lambda)$. Because $h_T \approx d_T + r^2/2R$ around the contact point, resonance wavelengths that depend linearly on h_T vary quadratically with *r* and create curved fringes in the SFA spectrograms with a parabolic tip corresponding to the contact point. In the spectrogram of Figure 2b, the intensity was measured at the contact position ($r = 0$) while increasing the surface distance d_T at a constant speed *u* of a few nms^{-1} using a motorized actuator (Figure 1). In this case, the intensity I_0 was resolved as a 2D-function of λ and time. Because $d_T(t) = d_0 + ut$, where d_0 is the initial thickness, each vertical line in the spectrogram corresponds to a specific time *t* and surface distance $d_T(t)$. The advantage of this approach is that the SFA can vary d_T dynamically and continuously over a wide range of surface distances, from several µm to direct surface contact ($d_T < 1$ nm for molecularly smooth surfaces), with an accuracy better than 1 nm and execution time of the order of minutes. To vary d_T, the surfaces were approached to or separated from each other at a constant speed. By recording $I_0(\lambda, t)$, the SFA allowed studying the

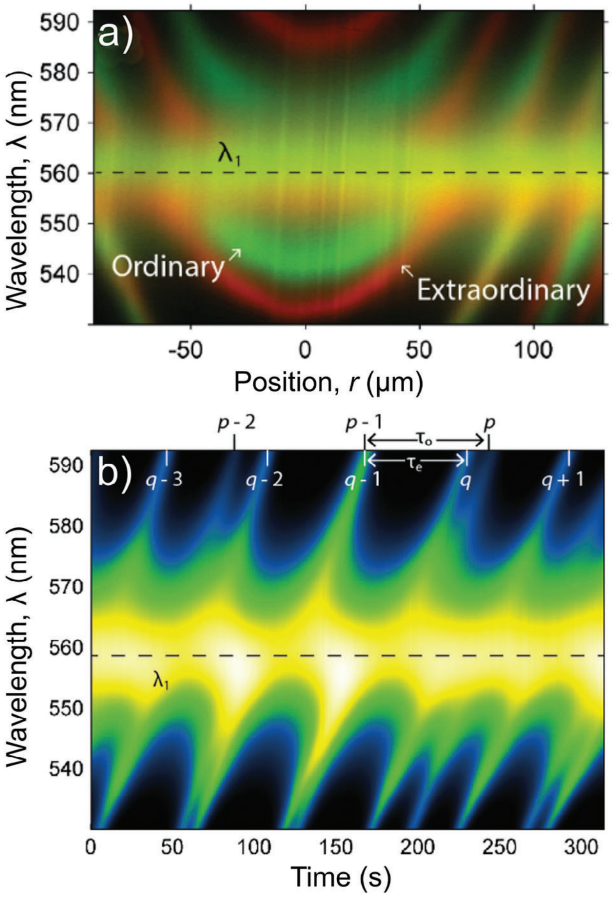

Figure 2. a) Transmitted intensity *T* measured for the MIMTMIM resonator in the SFA as a function of the wavelength λ and lateral distance *r* from the surface contact position ($r = 0$). Green and red fringes correspond to ordinary and extraordinary polarization, respectively, and were obtained by setting a linear polarizer perpendicular or parallel to the planar LC anchoring direction. The two fringe types overlap in the yellow regions, corresponding to the first-order resonance wavelength λ_1 of the MIM cavities. b) Transmitted intensity measured at the contact position ($r = 0$) as a function of time *t* and wavelength λ while separating the surfaces at constant speed *u*. Each value of *t* corresponds to a different separation distance (i.e., LC film thickness): $d_T = d_0 + ut$, where d_0 is the initial surface separation and *u* is the (constant) speed of surface separation. The mode order for ordinary and extraordinary fringes is denoted as *q* and *p*, respectively. A fringe with order *q* (or *p*) exits the spectral range at wavelength $\lambda = 593.2$ nm after a time τ compared to the fringe with order $q - 1$ (or $p - 1$). The delay is $\tau_o = 78.35$ s and $\tau_e = 60.85$ s for ordinary and extraordinary fringes, respectively.

resonance dispersion as a function of the cavity thickness d_T in a single sweep of thickness, instead of fabricating multiple cavities with different thicknesses. In the spectrograms of Figure 2a,b, the first-order resonance of the fixed-thickness MIM cavities produces a specific resonance wavelength λ_1 that does not depend on the thickness (d_T or h_T) of the MTM cavity, i.e., the LC film. On the other hand, the other fringes in the spectrogram are due to resonances of the MTM cavity and, therefore, depend both on the film thickness and polarization of the incident light. For a fixed surface distance (d_T or h_T) and far from λ_1, these fringes show an approximately parabolic shape (Figure 2a) reflecting the surface curvature, as expected. Due to the LC birefringence, these fringes form two distinct sets that can be separately extinguished using a linear polarizer parallel or perpendicular to the planar anchoring direction, as shown in Figure 2a (see also an example of unpolarized spectrogram in Figure S2, Supporting Information). This finding demonstrates that the resonance modes of the MTM cavity are linearly polarized along the ordinary and extraordinary axis of the uniformly aligned LC. The extraordinary modes appear slightly brighter than the ordinary ones (Figure S2, Supporting Information), because light was directed into the spectrograph using a right-angle mirror with polarization-dependent reflectivity (Figure S1, Supporting Information). This allows to identify the fringe polarization even though we cannot use a polarizer to dynamically resolve the polarization while varying d_T. Figure 2b shows that extraordinary fringes enter and exit the spectral range of the SFA (at a wavelengths distant from λ_1) more rapidly than ordinary fringes. In the entrance and exit regions, resonances approximately follow Equation (1). Therefore, if the mode with order q resonates at a given wavelength λ_1, then the mode with order $q \pm r$ resonates at the same wavelength after displacing the surfaces by a distance $\Delta d = \pm r\lambda_1/2n$. As a result of the inequality $n_e > n_o$, extraordinary fringes with index n_e cross the wavelength λ_1 more often than ordinary fringes as the distance d_T is increased. If the surfaces are separated at a constant speed u, the fringe with order q exits the spectral range after a time $\tau = \Delta d/u$ compared to the fringe with order $q - 1$. Figure 2b shows ordinary fringes exiting the spectral range at wavelength 593.2 nm at periodic time intervals $\tau_o = 78.3$ s, whereas the period is $\tau_e = 60.8$ s for extraordinary fringes. The ratio of these two periods, $\tau_0/\tau_e = 1.29$, is in good agreement with the value $\tau_o/\tau_e = n_e/n_o = 1.27$ predicted by Equation (1) using the nominal refractive indices (at room temperature) $n_e = 1.96$ and $n_o = 1.54$ of the LC. **Figures 3**a,b show intensity spectrograms $I_0(\lambda, t)$ obtained for the ordinary and extraordinary polarization, respectively, by using a polarizer in transmission. Resonance wavelengths are highlighted by black dashed lines and are referred to as λ_1, λ_U, and λ_L. As the thickness d_T of the LC film increases, λ_U approaches λ_1 while λ_L departs from λ_1. Eventually, λ_U and λ_L become equally spaced from λ_1 by a distance Ω. This behavior agrees with the numerical prediction and demonstrates the possibility of dynamically tuning the modes at different wavelengths ranging from 530 to 590 nm by acting on LC thickness or incoming light polarization. The MIMTMIM system studied in this work presents ENZ resonances for both LC thicknesses (134 and 100 nm) and refractive indices (n_o and n_e). This is confirmed by the effective dielectric constant that has been evaluated using the effective medium theory (EMT),[47] as reported in Figure S3 (Supporting Information). Moreover, the phase after propagation (through the whole resonator) was found to be $\phi \rightarrow 0$ meaning that $n \rightarrow 0$ at the resonant wavelengths as shown in Figure S3 b,d, Supporting Information). It is also important to note that when the phase goes toward zero, the phase velocity becomes infinite, indicating that the electromagnetic wave "tunnels" through ENZ material, enabling high transmission.[18,48]

4. Tuning Mode Coupling via LC Confinement and Reorientation

In order to understand why mode coupling produces a wavelength triplet, we calculated the transmitted intensity as a function of wavelength λ and LC film thickness d_T using the TMM method (**Figure 4**a), and selected three different values of d_T to compute, by a finite element method (COMSOL), the electric field map along the direction perpendicular to the MIMTMIM resonator as a function of λ and z position[2] (Figure 4b–e).

For $d_T = 100$ nm and ordinary polarization (Figure 4b), the high-energy mode has wavelength $\lambda_U^o \approx 450$ nm and is farther away from λ_1 than the low-energy mode with wavelength $\lambda_L^o \approx 585$ nm. This unequal wavelength spacing is reflected in mode hybridization. Namely, the high-energy mode is mainly located in the central MTM cavity while the low-energy mode is more delocalized among the central and outer (MIM) cavities. When the LC film thickness is increased to $d_T = 134$ nm (Figure 4c), the high-energy wavelength (Figure 4c) $\lambda_U^o \approx 510$ nm and low-energy wavelength $\lambda_L^o \approx 620$ nm are almost equally spaced from λ_1 and show a comparable degree of delocalization. When the LC film thickness is further increased to $d_T = 160$ nm (Figure 4d), the situation shown in Figure 4b is reversed and the high-energy mode at $\lambda_U^o \approx 530$ nm is closer to λ_1 and more delocalized than the low-energy mode at $\lambda_L^o \approx 670$ nm. Mode hybridization in MIMTMIM resonator can be understood based on its mirror symmetry under reflection on the middle plane of the central T-cavity. Symmetry requires that resonances be either even (+) or odd (-) under reflection (Figure 4b–e). Using first-order perturbation theory or variational method,[42,49] these modes can be approximated as symmetry-adapted linear combinations of single-cavity modes. In particular, the field E_c of first-order mode in the central cavity is even and, therefore, hybridizes with the field E_+ of the even combination of outer-cavity modes. Against, the odd combination E_- cannot hybridize with an even mode such as E_c. While the modes E_c and E_+ overlap and interfere with each other, particularly within the metal layers of the central MTM cavity, direct overlap and interference between the outer cavities is negligible and, as a result, the wavelength λ_- of the E_- mode is very close to the wavelength λ_1 of an isolated MIM cavity. Indeed, the difference between λ_- and λ_1 was too small to be detected in our experiments.

Hybridization between same-parity modes produces the wavelengths λ_L and λ_U observed both in the SFA experiments and in our calculation.[42] For first-order modes, these wavelengths correspond to the modes $E_L = E_c + \alpha E_+$ and $E_U = E_c - \beta E_+$, respectively, where the positive linear coefficients α and β depend on the thickness d_T of the central MTM cavity. The wavelengths λ_L and λ_U are due to the anti-crossing interaction between the even mode E_c and E_+ occurring as d_T varies (Figure 4b,d). Namely, the E_U-mode repels the E_L-mode as it moves toward lower energies, while the E_- mode is unaffected. The avoided-crossing point is

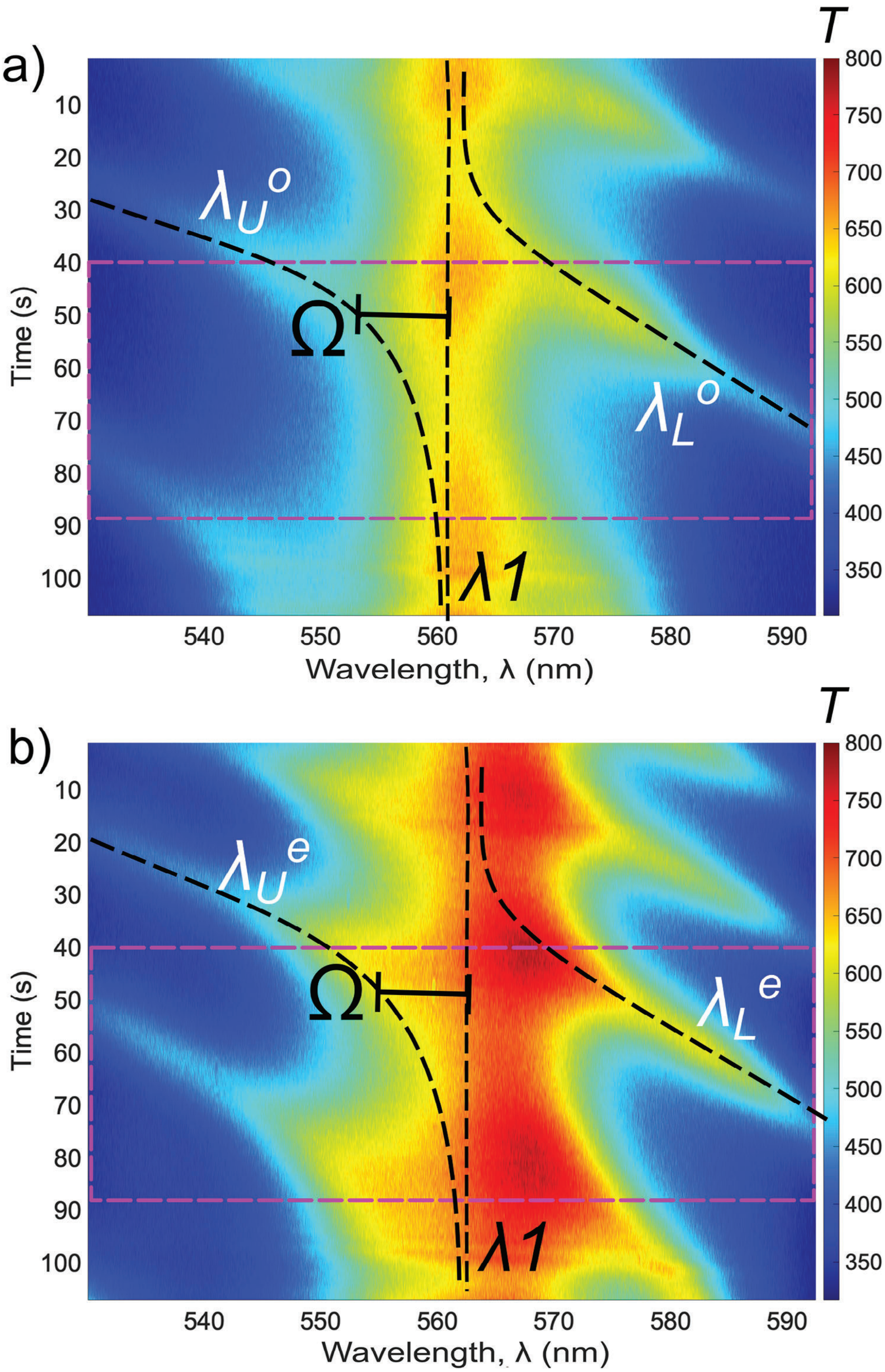

Figure 3. Light intensity T transmitted through the system measured for a) ordinary and b) extraordinary polarizations as a function of the wavelength λ and time t during surface separation (LC cavity expansion) with constant surface speed u. The maps show the resonance wavelengths λ_U and λ_L obtained during the surface separation together with their separation Ω from the resonance λ_1.

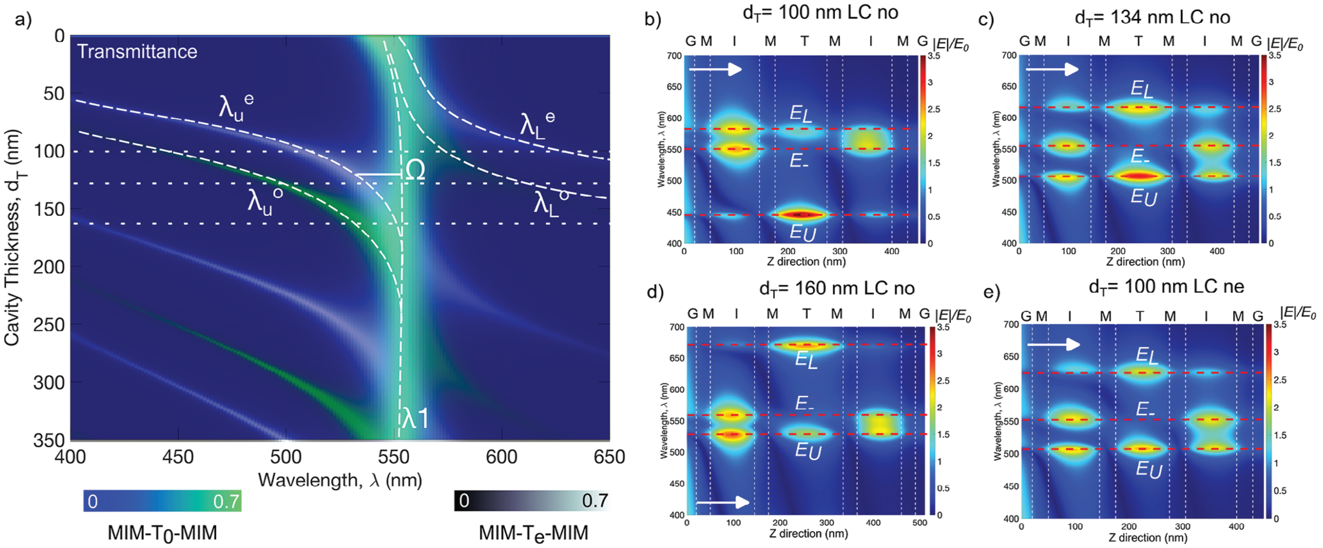

Figure 4. a) Calculated spectrogram showing the transmitted intensity as a function of the wavelength λ and of the LC cavity thickness d_T for both ordinary (blue-to-green colormap in the bottom left corner) and extraordinary polarizations (black-to-dark cyan colormap in the bottom right corner). b,d) Normalized electric field amplitude ($|E|/E_0$) calculated for the ordinary polarization (LC$_{no}$) as a function of the position z along the surface normal of the MIMTMIM resonator and wavelength λ. The considered cavity thickness d_T is indicated above each image. e) Electric field calculated for d_T = 100 nm and extraordinary polarization (LC$_{ne}$). The white dotted vertical lines mark the metal-dielectric interfaces, G (glass) is the medium outside the resonators. The white arrow shows the direction of incidence.

reached when the wavelength λ_q of the E_c-mode (Equation (1)) overlaps with the first-order wavelength λ_1 of the outer MIM cavities. In other words, the difference or "detuning" between the photon energies of the two modes becomes zero. At this point, the modes E_L and E_U become uniformly delocalized across the resonator, with equal intensity maxima in each cavity (α, $\beta \approx 1$, Figure 4c). At the avoided-crossing point, the wavelengths λ_L and λ_U are found at an equal distance Ω from the wavelength λ_1 of the $E\_$ mode.

A decisive advantage of using an anisotropic LC film is that the detuning can be actively controlled not only by varying the MTM cavity thickness, but also by selecting the refractive index of the LC. This fact is highlighted in Equation (1) showing that the resonance wavelength λ_q depends on the product $n_T d_T$ and, therefore, the thickness d_T and index n_T play equivalent roles. For example, the transmittance variation obtained by increasing the film thickness from d_T = 100 nm (Figure 4b) to d_T = 134 nm (Figure 4c) can also be obtained by switching the refractive index from ordinary to extraordinary (Figure 4d) while keeping the film thickness fixed to d_T = 100 nm. The switching can be obtained by changing the polarization from ordinary to extraordinary, or acting on the LC orientation (e.g., by applying a voltage to the silver surfaces of the MTM cavity) so as to vary the refractive index seen by extraordinary waves.

As a further demonstration of mode hybridization, the electric field was calculated using finite element method for the three LC thicknesses under normal incidence in Figures S4 and S5 (Supporting Information) the transmittance plots, electric field confinement into the LC cavity (n_e), and electric field distributions along the propagation direction are also shown.

In **Figure** 5a, the wavelength splitting 2Ω related to the difference $\lambda_L - \lambda_U$, $\lambda_1 - \lambda_U$ and $\lambda_1 - \lambda_L$ is shown as a function of the LC thickness. The top and bottom panels show the resonance wavelengths retrieved via a multiple Gaussian fit on the transmittance curves, for the anti-crossing behavior represented by λ_U approaching λ_L, λ_U approaching λ_1, and λ_1 approaching λ_L, for the ordinary and extraordinary LC refractive index, respectively. The minimum value of 2Ω corresponds to the avoided-crossing point and maximum coupling between same-parity modes. The same behavior is observed in experiments (Figure 5b). The slight difference related to the amplitude (2Ω) reported in both plots, numerical and experimental ones, for extraordinary polarization is a consequence of the non negligible effect of changing the surrounding medium around the two MIM resonators. In Supporting Information, we also simulated the angular dependence by varying the incident angle θ_i from 0° to 80° in steps of 2° for both ordinary and extraordinary polarization (Figure S6, Supporting Information). The results show that the three-cavity resonator is not significantly perturbed by the variation of the incident angle, especially for the extraordinary polarization.

5. Conclusion

In conclusion, we presented a detailed study on how to design and actively tune strongly confined hybrid modes in 1D layered structures working in visible wavelengths. The active control is enabled by a high-birefringence LC in combination with an SFA that can vary the cavity thickness rapidly, continuously, and accurately from several µm down to direct contact between its metal mirror surfaces. Importantly, we studied numerically and experimentally how the system performs in terms of weak and strong light coupling conditions when an LC film is confined between two MIM cavities. This result has significant practical implications for the development of innovative devices as it enables the possibility to excite multiple resonant modes across the LC cavity. This is of fundamental importance for developing

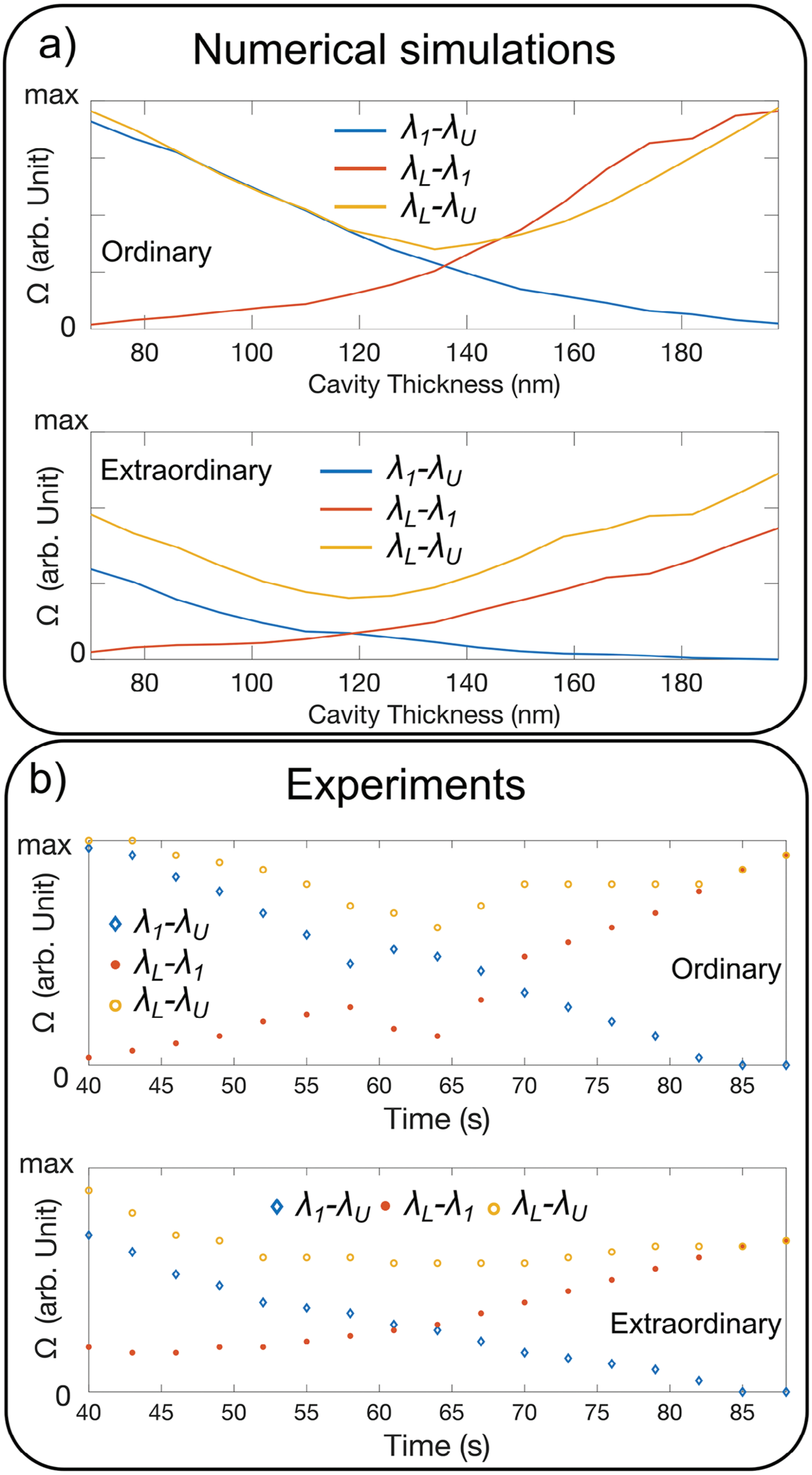

Figure 5. a) Numerical and b) experimental distance 2Ω between the wavelengths λ_L and λ_U for ordinary (top panels) and extraordinary (bottom panels) polarizations calculated for the following resonant mode conditions: λ_U approaches λ_1, λ_L, departs from λ_1 and λ_U approaches λ_L (anti-crossing).

active and reconfigurable devices that can find applications as a platform for optical beam steering devices. Thanks to the tunability of these photonic modes, the proposed system can be of extremely high importance for bio-sensing where it is necessary to involve high energy modes (short wavelengths, from 450 to 530 nm) excitable in free-space. Although the cavity resonances were obtained under normal incidence, it is expected that plasmonic modes can also be excited in a multi-cavity metamaterials under oblique incidence, notably without using any coupler (i.e., a grating) to generate evanescent waves. To this end, the SFA could be used to study the generation, coupling, and transmission of plasmonic modes in multi-cavity metamaterials as a function of the thickness and refractive index of LC loaded cavity.

6. Experimental Section

Sample Fabrication: The MIM cavities were fabricated by DC/RF sputtering (model Kenosistec KC300C), and they were constituted of Ag and transparent Zinc-oxide (ZnO), respectively with target thickness of 30 and 95 nm, on cylindrical glass lenses. The lenses had a diameter of R = 2 cm , the thickness of 4 mm, 60/ 40 scratch/dig surface quality, centration wedge angle <5 arcmin, and irregularity (interferometer fringes) $\lambda/2$ at a wavelength of 630 nm. Ag was chosen for its large extinction coefficient $k > 1 \gg n$, ensuring a high reflectivity and an approximately real negative permittivity in the metal layers while ZnO was chosen for its transparency ($n > 1 \gg k$). For the deposition, the following parameters were used: vacuum $7 \cdot 10^{-6}$, DC power 100W for 62s for Ag layer while ZnO were deposited using the RF cathode at a power of 80W and time of 31min 36s. In order to align the LC layer, a solution photo-active poly(amide imide), denominated JK158 in N-methylpyrrolidone (1 wt.%) was spin-coated on top of the exposed Ag layers at 3500 rpm for 45 s followed by a baking a 65°C for 3 h to evaporate the solvent. Finally, the JK158 film was irradiated through a linear polarizer with a light source having wavelength of 365nm (UV-Kub 2, KLOE') for 30 min. The poly(amide imide) was described in ref. [50]. JK158 contains randomly aligned azo-dye molecules that reorient perpendicularly to the polarization direction of UV light to minimize the absorption cross-section. The LCs in contact with the aligned JK158 molecules acquire the same alignment.

The Surface Forces Apparatus: A surface forces apparatus (SFA) Mark III by Surforce LLC, USA was used for the experiments.[42,51] One of the MIM-coated cylindrical lenses was fixed on a rigid support, whereas the other was attached to the free end of a double cantilever spring. The opposite end was rigidly attached to a motorized precision actuator performing controlled displacements with a known uniform speed u of a few nms^{-1}. A LC droplet with a volume of 50 µL was infiltrated between the surfaces by capillarity.

Transmission spectra were obtained by illuminating the surfaces under normal incidence with white light from a halogen lamp. The transmitted light was collected through the entrance slit of an imaging spectrograph (PI Acton Spectra Pro 2300i) aligned with one of the cylindrical lenses and recorded with a high-sensitivity CCD camera (Andor Newton DU940P-FI).

The separation distance between the crossed cylindrical surfaces, equal to the LC film thickness, was $h_T \simeq d_T + r^2/2R$, where r was the lateral distance from the surface contact position ($r = 0$), d_T was the surface distance at the contact position, and $R = 2$ cm was the cylinder radius (Figure 1a,b). The film thickness h_T depended on r as in a sphere-plane geometry because the camera probed a small surface region surrounding the contact position, such that $r \leqslant 0.15$ mm $\ll R$.[52]

The SFA provided a passive geometry-based method and an active displacement-based method for studying the effects of film thickness variations. In the passive method, the surfaces were kept at a constant surface distance d_T. The CCD camera recorded the transmitted intensity as a 2d function $I(\lambda, r)$ of the wavelength λ and distance r along the spectrograph entrance slit. Because the dependence of h_T on r was known, intensity variations along the r-axis could be immediately related to known variations of h_T. The image in Figure 2a is a 2d spectrogram produced with this method.

In the active method, the CCD records a video with acquisition rate of (1–3) images per second while varying the surface distance d_T at a constant speed. The intensity spectrum $I(\lambda, 0)$ at the contact position was selected from each image, and the spectra were stacked in 2d spectrogram $I(\lambda, t)$, where t is the spectrum acquisition time. The spectrogram in Figures 2b was obtained with this method. In both methods, resonances due to constructive multi-beam interference within the cavities appeared as intensity peaks in the spectrograms, i.e., local maxima of 2d intensity functions.

Before starting a measurement, the SFA was equilibrated for at least 1 h at 25.0 °C to reduce unwanted thermal or mechanical drifts of the distance d_T below 5 nmmin^{-1}. To obtain uniform d_T variations, the fixed cantilever end was displaced at a controlled speed of a few nms^{-1} using a motorized precision actuator. Because the surfaces were well separated from each other and did not interact mechanically, the cantilever moved without deflecting and, therefore, the distance d_T varied by an amount equal to cantilever displacement.

Numerical Simulations: The transfer matrix method (TMM) analysis were performed using a script implemented in commercial software Matlab. It uses as input the refractive indices data, the layer thicknesses and it allows calculating the spectrum varying the T cavity thickness. The refractive indices of Silver and Zinc Oxide were retrieved with Woollam M2000 ellipsometer. They were already reported in the supporting Information of the previous manuscript including a link to an open repository of such data.[14]

Finete Element Method (FEM) simulation were performed using COMSOL Multiphysics with the same scheme reported in ref. [2]. In order to analyze the electric filed $|E|/E_0$, where E_0 had been calculated as $E_0 = \sqrt{(P/w)Z_0}$, here P is the input power ($1\,Wm^{-2}$), w represents the area illuminated by the light beam and Z0 is the impedance, in the MIMTMIM system a 1D cutting line had been used to collect the normalized electric filed as function of the structure size and wavelengths. The cutting line had been chose to cover the entire length of the MIMTMIM system plus extra 20 nm in the glass before and after the structure.

Supporting Information

Supporting Information is available from the Wiley Online Library or from the author.

Acknowledgements

This research was performed in the framework of the bilateral (Italy-Poland) project: "Active metamaterials based on new generation liquid crystals (LCMETA)" funded by the Italian Ministry of Foreign Affairs and International Cooperation and the Polish National Agency for Academic Exchange NAWA. G.E.L and F.R. thank the FASPEC (Fiber-Based Planar Antennas for Biosensing and Diagnostics) - supported by Tuscany region in the Horizon 2020 framework - and the project "Complex Photonic Systems (DFM.AD005. 317)". G.E.L. also thanks the research project "FSE-REACT EU" financed by National Social Fund - National Operative Research Program and Innovation 2014-2020 (DM 1062/2021). A.F and R.C thank the project "DEMETRA – Sviluppo di tecnologie di materiali e di tracciabilitá per la sicurezza e la qualitá dei cibi" PON ARS01 00401. R.K. and J.P. acknowledged the financial support from the MUT University Grant UGB 22 804 from funds for year 2023.

Conflict of Interest

The authors declare no conflict of interest.

Author Contributions

G.E.L. and A.F. contributed equally to this work and wrote the article. G.E.L and R.C. conceived the main idea in the framework of the research project "LCMETA". G.E.L and A.F. performed numerical simulations and samples fabrication. B.Z. performed the SFA measurements and provided theoretical explanations. E.S-B. synthesized and delivered LC photoaligning materials and supported the work with fundamental technical advice. R.K. tested photo-aligning materials. J.P., R.K., C.P.U., F.R., and R.C. provided fundamental support thanks to their expertize in liquid crystals. F.R. provided his expertise on light coupling behavior in complex media to explain the physics behind this work. All authors revised the paper and accepted its contents.

Data Availability Statement

The data that support the findings of this study are available from the corresponding author upon reasonable request.

Keywords

ENZ, high-birefringence liquid crystal, liquid crystals, metamaterials, nano optical-cavities

Received: October 23, 2023
Published online:

---

[1] F. Réveret, P. Disseix, J. Leymarie, A. Vasson, F. Semond, M. Leroux, J. Massies, *Phys. Rev. B* **2008**, *77*, 195303.
[2] G. E. Lio, G. Palermo, R. Caputo, A. De Luca, *RSC Adv.* **2019**, *9*, 21429.
[3] J. Cao, S. De Liberato, A. V. Kavokin, *New J. Phys.* **2021**, *23*, 113015.
[4] S. M. Choudhury, A. Shaltout, V. M. Shalaev, A. V. Kildishev, A. Boltasseva, in *CLEO: QELS_Fundamental Science*, Optical Society of America, Washington, DC **2016**, pp. FF1D–8.
[5] G. E. Lio, A. Ferraro, M. Giocondo, R. Caputo, A. De Luca, *Adv. Opt. Mater.* **2020**, *8*, 2000487.
[6] Z. Guo, H. Jiang, K. Zhu, Y. Sun, Y. Li, H. Chen, *Phys. Rev. Appl.* **2018**, *10*, 064048.
[7] G. E. Lio, A. Ferraro, T. Ritacco, D. M. Aceti, A. De Luca, M. Giocondo, R. Caputo, *Adv. Mater.* **2021**, *33*, 2008644.
[8] A. M. Shaltout, N. Kinsey, J. Kim, R. Chandrasekar, J. C. Ndukaife, A. Boltasseva, V. M. Shalaev, *Proc. IEEE* **2016**, *104*, 2270.
[9] R. Kowerdziej, A. Ferraro, D. C. Zografopoulos, R. Caputo, *Adv. Opt. Mater.* **2022**, *10*, 2200750.
[10] P. N. Dyachenko, S. Molesky, A. Y. Petrov, M. Störmer, T. Krekeler, S. Lang, M. Ritter, Z. Jacob, M. Eich, *Nat. Commun.* **2016**, *7*, 1.
[11] A. Ferraro, G. E. Lio, A. Hmina, G. Palermo, J. M. Djouda, T. Maurer, R. Caputo, *Nanophotonics* **2021**, *10*, 3907.
[12] K. V. Sreekanth, Y. Alapan, M. ElKabbash, E. Ilker, M. Hinczewski, U. A. Gurkan, A. De Luca, G. Strangi, *Nat. Mater.* **2016**, *15*, 621.
[13] K. V. Sreekanth, S. Zeng, K.-T. Yong, T. Yu, *Sens. Actuators, B* **2013**, *182*, 424.
[14] G. E. Lio, A. Ferraro, R. Kowerdziej, A. O. Govorov, Z. Wang, R. Caputo, *Adv. Opt. Mater.* **2023**, *11*, 2203123.
[15] A. Ferraro, G. E. Lio, M. D. L. Bruno, S. Nocentini, M. P. De Santo, D. S. Wiersma, F. Riboli, R. Caputo, R. C. Barberi, *Adv. Mater. Technol.* **2022**, *8*, 2201010.
[16] S. Vassant, J.-P. Hugonin, F. Marquier, J.-J. Greffet, *Opt. Express* **2012**, *20*, 23971.
[17] O. Reshef, I. De Leon, M. Z. Alam, R. W. Boyd, *Nat. Rev. Mater.* **2019**, *4*, 535.
[18] J. Wu, Z. T. Xie, Y. Sha, H. Fu, Q. Li, *Photonics Res.* **2021**, *9*, 1616.
[19] P. Jin, R. Ziolkowski, *IET Microw., Antennas propag.* **2010**, *4*, 1016.
[20] Z. Li, S. Butun, K. Aydin, *Acs Photonics* **2015**, *2*, 183.
[21] M. Heydari, M. Sabaeian, *Appl. Opt.* **2017**, *56*, 1917.
[22] A. Imamog, D. D. Awschalom, G. Burkard, D. P. DiVincenzo, D. Loss, M. Sherwin, A. Small, *Phys. Rev. Lett.* **1999**, *83*, 4204.
[23] A. D. Greentree, C. Tahan, J. H. Cole, L. C. Hollenberg, *Nat. Phys.* **2006**, *2*, 856.
[24] A. Patra, V. Caligiuri, B. Zappone, R. Krahne, A. De Luca, *Nano Lett.* **2023**, *23*, 1489.
[25] K. J. Vahala, *Nature* **2003**, *424*, 839.
[26] F. Liang, N. Clarke, P. Patel, M. Loncar, Q. Quan, *Opt. Express* **2013**, *21*, 32306.
[27] A. Frisk Kockum, A. Miranowicz, S. De Liberato, S. Savasta, F. Nori, *Nat. Rev. Phys.* **2019**, *1*, 19.
[28] T. Herzog, S. Böhrkircher, S. Both, M. Fischer, R. Sittig, M. Jetter, S. Portalupi, T. Weiss, P. Michler, *Phys. Rev. B* **2020**, *102*, 235306.
[29] K. C. Smith, Y. Chen, A. Majumdar, D. J. Masiello, *Phys. Rev. Appl.* **2020**, *13*, 044041.
[30] T. Cui, B. Bai, H.-B. Sun, *Adv. Funct. Mater.* **2019**, *29*, 1806692.
[31] I. De Bellis, D. Martella, C. Parmeggiani, D. S. Wiersma, S. Nocentini, *Adv. Funct. Mater.* **2023**, *33*, 2213162.
[32] I. Zubritskaya, R. Cichelero, I. Faniayeu, D. Martella, S. Nocentini, P. Rudquist, D. S. Wiersma, M. L. Brongersma, *Adv. Mater.* **2023**, *35*, 2209152.
[33] M. Sharma, T. Ellenbogen, *Laser Photonics Rev.* **2020**, *14*, 2000253.
[34] G. E. Lio, A. Ferraro, *Photonics* **2021**, *8*, 3.
[35] J. Wang, K. Li, H. He, W. Cai, J. Liu, Z. Yin, Q. Mu, V. K. Hisao, D. Gérard, D. Luo, et al., *Laser Photonics Rev.* **2022**, 2100396.
[36] G. Palermo, A. Lininger, A. Guglielmelli, L. Ricciardi, G. Nicoletta, A. De Luca, J.-S. Park, S. W. D. Lim, M. L. Meretska, F. Capasso, et al., *ACS Nano* **2022**, *16*, 16539.
[37] R. Kowerdziej, J. Krupka, E. Nowinowski-Kruszelnicki, M. Olifierczuk, J. Parka, *Appl. Phys. Lett.* **2013**, *102*, 102904.
[38] D. C. Zografopoulos, A. Ferraro, R. Beccherelli, *Adv. Mater. Technol.* **2019**, *4*, 1800447.
[39] R. Kowerdziej, T. Stańczyk, J. Parka, *Liq. Cryst.* **2015**, *42*, 430.
[40] G. Isić, G. Sinatkas, D. C. Zografopoulos, B. Vasić, A. Ferraro, R. Beccherelli, E. E. Kriezis, M. Belić, *IEEE J. Sel. Top. Quantum Electron.* **2019**, *25*, 1.
[41] J. N. Israelachvili, P. M. McGuiggan, *J. Mater. Res.* **1990**, *5*, 2223.
[42] B. Zappone, V. Caligiuri, A. Patra, R. Krahne, A. De Luca, *ACS Photonics* **2021**, *8*, 3517.
[43] G. Fowles, *Modern optics*, Holt, New York **1989**.
[44] M. Born, E. Wolf, *Principles of optics: electromagnetic theory of propagation, interference and diffraction of light*, Elsevier, Amsterdam **2013**.
[45] R. Dkabrowski, P. Kula, J. Herman, *Crystals* **2013**, *3*, 443.
[46] R. Węgłowski, W. Piecek, A. Kozanecka-Szmigiel, J. Konieczkowska, E. Schab-Balcerzak, *Opt. Mater.* **2015**, *49*, 224.
[47] W. Cai, V. M. Shalaev, *Optical Metamaterials*, vol. *10*, Springer, Berlin **2010**.
[48] M. Silveirinha, N. Engheta, *Phys. Rev. Lett.* **2006**, *97*, 157403.
[49] V. Caligiuri, M. Palei, G. Biffi, R. Krahne, *Nanophotonics* **2019**, *8*, 1505.
[50] J. Konieczkowska, E. Schab-Balcerzak, M. Siwy, K. Switkowski, A. Kozanecka-Szmigiel, *Opt. Mater.* **2015**, *39*, 199.
[51] J. N. Israelachvili, P. M. McGuiggan, *J. Mater. Res.* **1990**, *5*, 2223.
[52] J. N. Israelachvili, *Intermolecular and surface forces*, Academic press, Cambridge **2011**.